

# Boron Nanoparticles with High Hydrogen Loading: Mechanism for B–H Binding and Potential for Improved Combustibility and Specific Impulse

Jesus Paulo L. Perez,<sup>†</sup> Brandon W. McMahon,<sup>†</sup> Jiang Yu,<sup>†</sup> Stefan Schneider,<sup>‡</sup> Jerry A. Boatz,<sup>‡</sup> Tom W. Hawkins,<sup>‡</sup> Parker D. McCrary,<sup>§</sup> Luis A. Flores,<sup>§</sup> Robin D. Rogers,<sup>§</sup> and Scott L. Anderson<sup>\*,†</sup>

<sup>†</sup>Department of Chemistry, University of Utah, 315 S 1400 E, Salt Lake City, Utah 84112, United States

<sup>‡</sup>Propellants Branch, Rocket Propulsion Division, Aerospace Systems Directorate, Air Force Research Laboratory, AFMC AFRL/RQRP, 10 East Saturn Boulevard, Edwards AFB, California 93524, United States

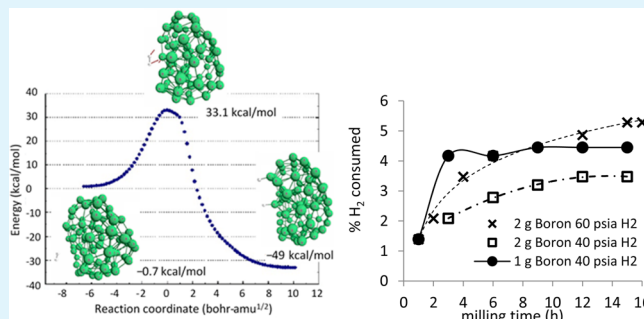
<sup>§</sup>Center for Green Manufacturing and Department of Chemistry, The University of Alabama, Tuscaloosa, Alabama 35487, United States

## Supporting Information

**ABSTRACT:** Ball milling of boron in an H<sub>2</sub> atmosphere was found to result in hydrogen uptake of up to 5% by weight (36 mol %). The nature of the hydrogen binding to boron was probed by a combination of ab initio theory, IR spectroscopy, thermogravimetric analysis, and mass spectral measurements of gases evolved during sample heating. The dominant binding mode is found to be H atoms bound to B atoms in the surface layer of the particles, and the high hydrogen loading results from production of very high surface area, indicating that gaseous H<sub>2</sub> is an effective agent promoting size reduction in milling. Hydrogen incorporated in the samples was found to be stable for at least a month under ambient conditions.

Desorption is observed beginning at ~60 °C and continuing as the temperature is increased, with broad desorption features peaking at ~250 and ~450 °C, and ending at ~800 °C. Unprotected hydrogenated boron nanoparticles were found to be reactive with O<sub>2</sub> producing a hydrated boron oxide surface layer that decomposed readily at 100 °C leading to desorption of H<sub>2</sub>O. Hydrogenated boron nanoparticles were found to promote a higher flame height in the hypergolic ignition of ionic liquids upon contact with nitric acid.

**KEYWORDS:** hydrogen enrichment, boron, mass spectroscopy, energetic materials



## INTRODUCTION

Boron's high heat of combustion makes it an interesting material for fuel and propellant applications,<sup>1</sup> but there are two issues that have frustrated wide use of boron in propulsion applications. One is a tendency to form HOBOR rather than the most stable B<sub>2</sub>O<sub>3</sub> product, with concomitant reduction in heat release. The other is simply that it can be difficult to achieve rapid ignition and complete consumption of boron particles. The work presented here is aimed at this latter issue. Boron is refractory, thus combustion is inherently a heterogeneous process, limited by the surface area of the boron particles. Reduction of boron into the nanoscale can, therefore, improve combustibility,<sup>2–4</sup> however formation of a refractory oxide layer on the particle surfaces upon air exposure impedes ignition and reduces the energy density. One approach to mitigating the effects of the oxide layer is to cap nanoparticulate boron with organic capping ligands, which protect the boron from premature oxidation, and control dispersibility in fuels/propellants.<sup>5–8</sup> Here, we examine a different approach to

improving boron's potential as a propellant—production of boron nanoparticles containing up to 5 wt % of hydrogen (~36 mol percent). Incorporation of hydrogen may have several effects. By reducing the average molecular weight of the combustion products, the specific impulse (*I*<sub>sp</sub>) would be improved, all else being equal.<sup>7</sup> In addition, given the fact that boranes (B<sub>*n*</sub>H<sub>*m*</sub> compounds) tend to be reactive with oxidizers,<sup>9</sup> hydrogenation might be expected to increase reactivity. Boron also has potential as a hydrogen storage material.<sup>10</sup> For example, diborane (B<sub>2</sub>H<sub>6</sub>) is 22 wt % hydrogen, surpassed only by methane (CH<sub>4</sub>, 25 wt %) in hydrogen content.

Hydrogen loading and adsorption properties of nanostructured solid boron compounds, such as BN<sup>11,12</sup> and MgB<sub>2</sub>,<sup>11</sup> have been studied recently. Tang et al.<sup>11</sup> measured as much as 5.6 wt % hydrogen loading on mesoporous BN

Received: March 7, 2014

Accepted: May 7, 2014

Published: May 7, 2014

nanotubes, while Pecharsky et al.<sup>11</sup> were able to load ~4 wt % hydrogen into powdered MgB<sub>2</sub> via ball milling methods. Fujii<sup>13</sup> attempted to hydrogenate elemental boron powder, also using ball milling, achieving 2.3 wt % hydrogen loading after 80 h milling under 10 atm of H<sub>2</sub>.<sup>13</sup> There is some precedence for use of hydrogenation to improve ignitability of diesel fuel,<sup>14</sup> and the effects of hydrogen loading on conventional hydrocarbon fuels such as gasoline,<sup>15</sup> jet fuel<sup>16</sup> and natural gas<sup>11,17,18</sup> has also been studied. Results suggest that thermal efficiency was increased and fuel consumption was reduced when the optimum proportion of hydrogen is added. Furthermore, evidence of reduced CO emission was also observed for hydrogen enriched fuels.<sup>11,16,19</sup>

Here, ball milling was used to prepare boron nanoparticles and load them with up to 5 wt % hydrogen—comparable to the DOE target for hydrogen storage systems (5.5 wt % by 2017).<sup>20</sup> The hydrogen remains in the boron samples when the H<sub>2</sub> pressure is removed, and we use a variety of theoretical, spectroscopic, and mass spectrometric methods to probe the nature of the hydrogen binding. The effects of air exposure are also probed, showing that the hydrogen-loaded boron does, indeed, oxidize more readily than boron prepared under inert atmosphere. The effect of hydrogenated boron loading on the hypergolic ignition of two ionic liquids was also tested, using white fuming nitric acid as the oxidizer.

## MATERIALS AND METHODS

**Hydrogen Loading and Nanoparticle Production.** Amorphous boron powder (~95%, 2 μm diameter) was purchased from C. R. Supply Co. (West Hills, CA) and used as received, although some experiments aimed at purifying the boron feedstock are discussed. Hydrogen loading was accomplished by milling boron powder in an H<sub>2</sub> atmosphere. In a typical milling procedure, 2 g of boron and 160 g of 1/8 in. diameter tungsten carbide media were loaded into a 500 mL tungsten carbide-lined milling jar. Tungsten carbide was adopted based on initial experiments with boron milling using stainless steel media and jars, where milling times had to be roughly doubled to reach the same particle size range, and the products contained high levels of ferrous metal contamination.

The jar lid was modified with two valved ports which allow the jar atmosphere to be pumped out, purged, filled, and sampled, without breaking the lid seal. Unless noted, all manipulations, including loading and unloading the jar, gas handling and sampling, and transfer of samples for various analyses, were performed in an N<sub>2</sub>-filled glovebox. After loading, the jar was sealed and then pumped out and purged with Ar three times, before finally pumping out the Ar and charging the jar with H<sub>2</sub> gas (99.95%). For most experiments the absolute H<sub>2</sub> charge pressure was 60 psia (~4 atm). Milling was done using a planetary ball mill (PM 400, Retsch, Inc.) for a total of 16 h at 300 rpm, with rotation direction reversed every 30 min. The H<sub>2</sub> pressure was monitored periodically during milling by connecting a gauge to one of the ports in the jar lid, pumping out the gauge to avoid air introduction. Similar procedures were used for D<sub>2</sub> loading experiments.

**Hydrogen Content Analysis.** The hydrogen content of samples was analyzed using a high-temperature-conversion elemental analyzer (TC/EA) coupled to an Isotope Ratio Mass Spectrometer (IRMS, Thermo Fisher Scientific) through an open split interface. A sample of the milled boron was transferred to a vial, and then dropped into a He stream, which carried the sample through a 1400 °C reactor, desorbing any hydrogen as H<sub>2</sub>. Gases were separated in a 1 m gas chromatography column (SA, 80 mL/min, 95 °C) before entering the IRMS for quantitation. Ultrahigh purity H<sub>2</sub> was injected for mass and sensitivity calibration. This instrument is not equipped for inert transfer, therefore the sample was exposed to air briefly as it was dropped into the He carrier stream.

**Electron Microscopy.** Particle size and shape were analyzed using scanning electron microscopy (SEM, FEI Nova Nano 600) and transmission electron microscopy (TEM, FEI Technai Osiris) with electron energy loss spectroscopy (EELS) to verify composition. Samples were prepared by sonicating and dispersing particles in ethanol to break up aggregates, then drop casting onto transmission electron microscopy (TEM) grids. All microscopy samples were exposed to air.

**Fourier Transform Infrared (FTIR) Analysis.** A Nicolet iSS FTIR spectrometer was used to collect infrared spectra using attenuated total reflectance (ATR), with samples pressed directly onto the instrument's diamond crystal. IR spectra are the average of 15 scans at 1 cm<sup>-1</sup> resolution.

**Mass Spectrometry Analysis.** After milling selected samples, headspace gas was analyzed using a quadrupole mass spectrometer system with base pressure below 10<sup>-8</sup> mbar. The gas was sampled into an evacuated glass tube connected to the milling jar's valve port, then connected to the inlet system of the mass spectrometer, without air exposure. Mass spectra were also measured for gases evolved from samples of H<sub>2</sub>- and D<sub>2</sub>-loaded boron nanoparticles as they were heated. For these measurements, the jar was opened in the glovebox, and a boron sample was collected and transferred into a glass sample tube equipped with a valve. The tube was then connected to the mass spectrometer inlet without air exposure, and gases evolved from the samples were continuously monitored as the sample was slowly heated to 350 °C in a tube furnace. The variation of sensitivity with mass was calibrated and corrected by measuring the intensities resulting from known pressures of H<sub>2</sub>, D<sub>2</sub>, and Ar.

**Tandem thermogravimetric-mass spectrometry analysis (TGA-MS).** Mass losses as a function of temperature was analyzed with a TA Instruments Q500 Thermogravimetric Analyzer (TGA) operated inside a N<sub>2</sub>-filled glovebox, so that samples could be studied without air exposure. Samples were heated from 25 to 900 °C at 10 °C/min under N<sub>2</sub> gas flow (90 mL/min). The gas stream was analyzed using a Pfeiffer ThermoStar quadrupole mass spectrometer. Oxidation of boron samples was studied using a TA Instrument 2950 TGA operated outside the glovebox with O<sub>2</sub> flowing through the furnace and sample balance. These samples were exposed to air during transfer to the instrument, and this instrument was not equipped with a mass spectrometer.

**Theoretical Performance Calculation.** One potential application is as a fuel additive in a bipropellant propulsion system. The theoretical performance gain from hydrogen loading was estimated using the US Air Force specific impulse computational code.<sup>21</sup>

**Density Functional Theory (DFT) Calculations.** The interactions between boron nanoparticles and hydrogen were computed using density functional theory (DFT) methods. A cluster of 80 boron atoms with both exposed surface atoms and a bulk-like core<sup>22,23</sup> was used as a model for the surface region of boron nanoparticles. The M06 hybrid meta-generalized gradient approximation (GGA) exchange-correlation functional of Zhao and Truhlar<sup>24</sup> was used in conjunction with the 6-311++G(d,p) basis set<sup>25,26</sup> for boron and hydrogen. All structures were fully optimized and verified as local minima or saddle points via diagonalization of the energy second derivatives with respect to mass-weighted nuclear displacements. A scale factor of 0.983<sup>24</sup> was used in computing infrared spectra and zero point vibrational energy corrections from the harmonic vibrational frequencies. All calculations were performed using the GAMESS<sup>27,28</sup> and NWChem<sup>29</sup> quantum chemistry programs.

**Synthesis of Ionic Liquids.** Two hypergolic ionic liquids (ILs), i.e. liquid organic salts which ignite upon contact with white fuming nitric acid,<sup>30</sup> were synthesized to test the combustion properties of the hydrogenated boron nanoparticles. The IL precursors, 1-butyl-3-methyl-imidazolium chloride and 1-methyl-4-amino-1,2,4-triazolium iodide were synthesized through typical quaternization reactions between heterocycles (1-methyl-imidazole and 4-amino-1,2,4-triazole) and alkylating agents (1-chlorobutane and methyl iodide).<sup>31</sup> Halide precursors were dissolved in the minimum amount of methanol and silver dicyanamide was added and stirred for 5 days. The resulting silver halide salts were filtered and methanol was removed by reduced

pressure to obtain 1-butyl-3-methyl-imidazolium dicyanamide ([BMIM][DCA]) and 1-methyl-4-amino-1,2,4-triazolium dicyanamide ([MAT][DCA]) as very slightly yellow liquids.<sup>30,31</sup> ILs were further dried at 70 °C for 7 days at  $10^{-4}$  Torr until they contained less than 2000 ppm of water. 1-methyl-imidazole was purchased from Sigma-Aldrich and used as received. 4-amino-1,2,4-triazole, 1-chlorobutane, methyl iodide, silver nitrate, and sodium dicyanamide were purchased from Alfa Aesar and used as received.

#### Stabilization of Hydrogenated Boron Nanoparticles in ILs.

Small portions of hydrogenated and deuterated boron nanoparticles (0.6–0.9 mg) were placed in preweighed vials while under an Ar atmosphere. [BMIM][DCA] or [MAT][DCA] were added to the vials in an argon glovebox to obtain 0.3 wt % suspensions. Mixtures were then sealed, brought out of the glovebox, and a Branson 5510 bath sonicator was used to disperse the particles, as described previously.<sup>31</sup> In each case, the suspensions produced a cloudy yellow color.

**Hypergolic Ignition Tests.** To determine the combustion and ignition properties of the hydrogenated boron nanoparticles, neat samples of hypergolic ILs were compared to samples of hypergolic ILs containing 0.3 wt % of hydrogenated boron nanoparticles. Aliquots (10  $\mu$ L) of neat ILs or ILs loaded with boron nanoparticles were added via Hamiltonian syringe to a flat bottom vial containing 500  $\mu$ L of 99% white fuming nitric acid, which followed our previously reported procedures.<sup>31</sup> The reaction was monitored for ignition delay (defined as the time from when the drop of IL hits the surface of the oxidizer until the resulting ignition), flame height, and ignition dynamics utilizing a Redlake MotionPro Y4 high speed camera at 1000 frames/s. Each test was repeated a total of three times to determine repeatability.

## RESULTS AND DISCUSSION

**Quantifying hydrogen loading in boron.** Hydrogen uptake was determined in two ways. Figure 1a shows the pressure drop inside the milling jar for three sets of conditions. Data are shown for milling of 2 g of boron in 60 psia (4 atm) initial  $H_2$  pressure, which dropped by a factor of about three during milling. For comparison, pressure vs time traces are also

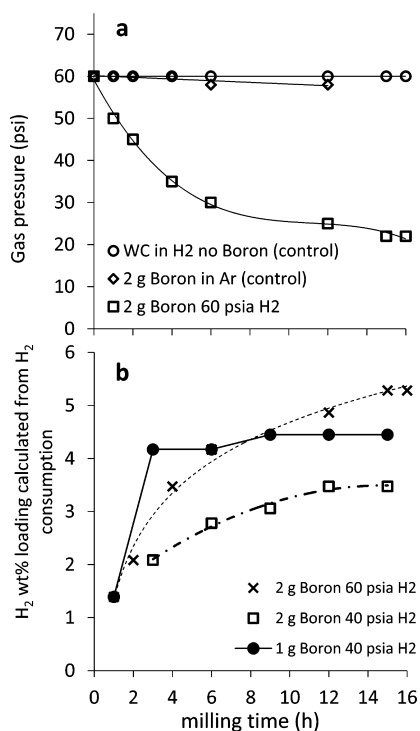


**Figure 1.** (a) Pressure drop of  $H_2$  inside the jar measured at different intervals during the milling. (b)  $H_2$  consumed during the milling as weight percent of boron loading.

shown for milling runs where either the boron was omitted, or the jar was filled with argon instead of  $H_2$ . In these two control runs, there was no pressure drop, showing that boron does not absorb argon significantly, that the jar seal is not permeable to  $H_2$ , and that the tungsten carbide media and jar lining do not absorb hydrogen.

Figure 1b summarizes experiments carried out with varying initial boron mass and  $H_2$  pressure, where the  $H_2$  pressure drops have been converted to the equivalent  $H_2$  uptake, that is,  $H_2$  consumed as a weight percent (wt %) of the initial boron mass. The  $H_2$  uptake varied from  $\sim 3$  wt % to  $\sim 5$  wt %, increasing with increasing ratio of  $H_2$  to boron in the initial jar loading. We did not attempt milling at higher  $H_2$  pressures because of limitations of the jar seal design, however, we note that the  $H_2$  uptakes observed here are higher than the 2–3 wt % hydrogen loadings observed in previous studies that used higher  $H_2$  pressures and much longer milling times (70–145 psi, 80–100 h).<sup>13,32</sup> To see if higher loadings could be obtained if the  $H_2$  pressure was maintained during milling, we tried periodically adding  $H_2$  to bring the jar pressure back to 60 psia, and also extended the milling time to 24 h but no additional uptake was observed.

An obvious question is whether the hydrogen taken up by the boron during milling remains in the sample when the  $H_2$  overpressure is removed. Therefore, we also measured the hydrogen content of one of the milled samples using TC/EA, as described above. The sample used in this analysis was one where the  $H_2$  loading calculated from the milling pressure drop was 3.4 wt %. TC/EA analysis found evolution of 3.5 wt % of  $H_2$  when the sample was heated to 1400 °C. It is important to note, however, that the TC/EA instrument is not equipped with an inert sample transfer system, thus the sample was briefly exposed to air. Air exposure might result in some hydrogen loss from the boron because of oxidation of the boron particle surface, but might also lead to uptake of hydrogen in the form of atmospheric water or other hydrogen-containing contaminants. Therefore, a sample of the unmilled boron feedstock was also analyzed by TC/EA, resulting in a measured hydrogen content of  $\sim 0.4$  wt %. The TC/EA analysis shows, therefore, that milling boron in  $H_2$  increased the hydrogen content by at least  $\sim 3.1$  wt %. The extra hydrogen content is slightly lower than the 3.4 wt % uptake inferred from the pressure drop during milling, however, lack of quantitative agreement is not surprising given the possible effects of air exposure prior to TC/EA analysis. We conclude, therefore, that the  $H_2$  pressure drop really does reflect some process by which  $H_2$  is taken up by the boron under milling conditions, binding in such a way that it is not lost under ambient conditions.

**Possible Modes of Hydrogen Uptake by Boron.** When considering how hydrogen might bind to boron in these samples, it is important to keep in mind that the amount of hydrogen is quite high, up to 5 wt % ( $\sim 36$  mol %), corresponding to a stoichiometry of 1 H atom for every  $\sim 1.8$  B atoms. The two obvious mechanisms for hydrogen uptake are binding of hydrogen to surface or interstitial sites of the nanoparticles, or reaction to form molecular boranes.

Formation of stable borane molecules could account for the observed pressure drops during milling. For example, if  $H_2$  reacted with boron to produce diborane gas ( $B_2H_6$ ), the pressure drop would be a factor of 3 (at 100% conversion), in reasonable agreement with our observation (Figure 1a). Formation of higher molecular weight boranes such as tetraborane ( $B_4H_{10(g)}$ ), pentaborane ( $B_5H_9(l)$ ), or decaborane

( $B_{10}H_{14(s)}$ ) would result in larger pressure drops, for a given extent of conversion. Most of these species have significant vapor pressures, and would be entirely or partially lost during the sample transfer for hydrogen content analysis by TC/EA (above). Simple boranes are also pyrophoric in sufficient concentrations, however, because we always sampled headspace gases and evacuated the jar before opening it (in an  $N_2$  glovebox), the absence of autoignition does not preclude borane formation during milling. Mass spectrometry to look for boranes is discussed below.

If hydrogen were to bind only to sites on the particle surfaces, the saturation coverage would likely be close to one H atom per surface B atom (see below). In that case,  $\sim 56\%$  of the B atoms would need to be in the surface layer, corresponding to  $\sim 1200 \text{ m}^2/\text{gram}$  of surface area. As discussed in the Supporting Information (Figure S1), if spherical, such particles would have an average diameter of  $\sim 2 \text{ nm}$ . If H or  $H_2$  can bind or be trapped in bulk interstitial sites, such as the  $B_{12}$  icosahedral sites known to exist in amorphous boron,<sup>33</sup> then the hydrogen uptake would not require such high surface area.

Density functional theory (DFT) calculations were conducted to assess the stability of various boron–hydrogen bonding arrangements, and the activation energies for their formation. The boron particle was represented by a  $B_{80}$  cluster which contains a variety of different boron surface sites, as well as bulk-like interstitial sites, as discussed in the Supporting Information (Figure S2 and accompanying discussion). We first examined the interaction of a single  $H_2$  molecule with various sites on the surface of  $B_{80}$ . Typical optimized structures and reaction coordinates are shown in Figure 2 and Supporting

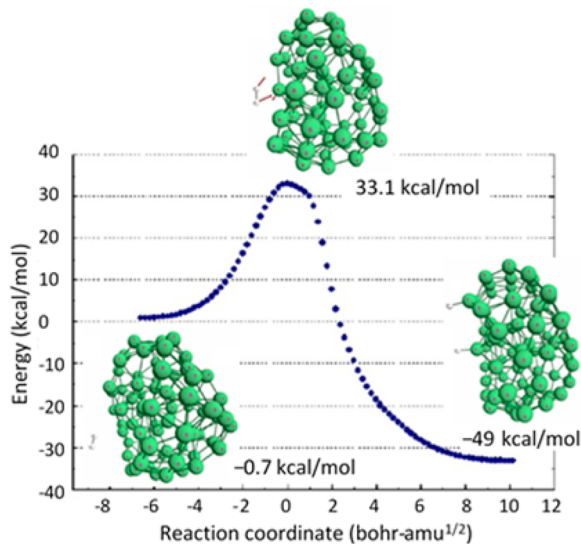


**Figure 2.** Reaction pathway and energy diagram for the interaction of an  $H_2$  molecule with a  $B_{80}$  cluster.

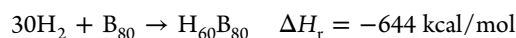
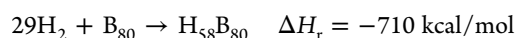
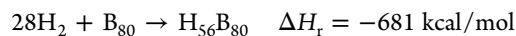
Information Figures S3–S10. Dissociative adsorption of hydrogen to form borane-like B–H bonds on adjacent B atoms is energetically favorable, with activation barriers in the 5–33 kcal/mol range, depending on which part of the  $B_{80}$  cluster is involved (Figure 2 and Supporting Information Figure S3–S7). As shown in these figures, the dissociative reaction pathways involve initial weak ( $<1 \text{ kcal/mol}$ ) long-range interaction of  $H_2$  with the cluster, and then initial attack of  $H_2$  on a single B atom, forming a transition state. The arrows shown on the transition state structures are the motions

corresponding to the single imaginary frequency at the transition state, i.e., the reaction coordinate. As the  $H_2$  dissociates to form B–H bonds on adjacent boron atoms, the B–B distance between these atoms also increases, effectively breaking the B–B bond.

For milling conditions, where the temperature approaches  $100 \text{ }^\circ\text{C}$ , such reactions should be facile. A molecularly bound  $H_2$ – $B_{80}$  complex was also observed (Supporting Information Figure S4); however, it is predicted to be energetically unfavorable and would dissociate back to  $H_2 + B_{80}$  at nonzero temperatures. Once an adsorbed  $H_2B_{80}$  complex is formed, the H atoms can migrate on the  $B_{80}$  surface, with activation barriers in the 1 to 22 kcal/mol range, depending on which sites are involved (Supporting Information Figures S5–S8). Complexes where one of the H atoms is bridge-bonded to a pair of B atoms were also observed (Supporting Information Figure S9), but these are higher in energy than complexes with both H atoms in terminal B–H bonds, and the activation barrier stabilizing the bridge-bonded structure is low ( $\sim 3 \text{ kcal/mol}$ ), suggesting that bridge bonded structures should be kinetically unstable. Supporting Information Figure S10 summarizes the structures of different  $H_2B_{80}$  isomorphs (with  $H_2$  dissociatively adsorbed) investigated, which were found to be stable with respect to  $H_2 + B_{80}$  reactants by between 3.5 and 60 kcal/mol.

The possibility of hydrogen binding into interstitial sites was also considered in these calculations. For  $H_2@B_{80}$ , i.e.,  $B_{80}$  containing a single  $H_2$  molecule trapped interstitially (Supporting Information Figure S11), the energy is found to be 62.7 kcal/mol above the  $H_2 + B_{80}$  reactants, however, if zero point energy is included, then this structure is unstable with respect to dissociation of the interstitial  $H_2$  to two interstitial H atoms. This structure with two interstitial H atoms is still 56.3 kcal/mol above  $H_2 + B_{80}$ , that is, far above the energies of structures with both H atoms bound on the  $B_{80}$  exterior. We also examined the energetics for migration of one of the exterior H atoms in  $H_2B_{80}$  migrating to an interstitial site, and found that the process is unfavorable by 57 kcal/mol, with a barrier of 58.4 kcal/mol. It seems clear, therefore, that when  $H_2$  attacks a clean boron surface, dissociative adsorption with both H atoms remaining on the surface, is far more energetically favorable than interstitial trapping of H,  $H_2$ , or 2 H. The possibility remains, however, that H or  $H_2$  might trap in interstitial sites after all the surface sites are saturated.

The process of saturating the  $B_{80}$  surface was probed via DFT calculations on  $H_xB_{80}$  ( $x = 56, 58$  and  $60$ ). The total energies with respect to  $(x/2)H_2 + B_{80}$  are as follows:



Optimized structures for  $H_{58}B_{80}$  and  $H_{60}B_{80}$  are shown in Supporting Information Figures S12 and S14. From the total energies above, we can calculate that the  $H_2$  addition reaction  $H_2 + H_{56}B_{80} \rightarrow H_{58}B_{80}$  is exoergic by 29 kcal/mol, whereas the subsequent addition  $H_2 + H_{58}B_{80} \rightarrow H_{60}B_{80}$  is endoergic by 66 kcal/mol, that is,  $H_{58}B_{80}$  represents saturation of the surface. The structure for  $H_{60}B_{80}$  shown in Supporting Information Figure S14 suggests that while bridging (B–H–B) bonds become more likely in saturated structures, terminal B–H bonding still predominates.

To examine the possibility of binding hydrogen interstitially after saturating the surface, the energy was calculated for  $H@H_{57}B_{80}$ , that is, for  $H_{58}B_{80}$  where one of the surface H atoms was moved into an interstitial site. The barrier for the H atom migration is 42.6 kcal/mol and the movement of an H atom from the surface to an interstitial site is 36.6 kcal/mol endoergic (Supporting Information Figures S12). Finally, to test the energetics for trapping  $H_2$  inside boron where the surface is already saturated with B–H bonds, energetics were calculated for  $H_2@H_{58}B_{80}$  and  $H_2@H_{60}B_{80}$  (Supporting Information Figures S13 and S15). The energy for  $H_2@H_{58}B_{80}$  is 74.2 kcal/mol above  $H_2 + H_{58}B_{80}$ , however, if zero point energy is included, then the barrier for dissociation of the interstitial  $H_2$  vanishes, and one of the resulting H atoms emerges to the surface, generating  $H@H_{59}B_{80}$ , with an energy 28 kcal/mol above  $H_2 + H_{58}B_{80}$ . The energy for  $H_2@H_{60}B_{80}$  is 35 kcal/mol above  $H_2 + H_{60}B_{80}$ , but note that  $H_{60}B_{80}$  is already metastable by 66 kcal/mol with respect to  $H_2 + H_{58}B_{80}$ .

In summary, the theory clearly shows that surface B–H binding, up to a saturation level approaching one H atom per surface boron atom, is energetically favorable, with activation energies in a range that should allow facile reaction at the <100 °C temperatures range of the mill. Interstitial binding is far less energetically favorable, and metastable with respect to migration to surface sites. Theory, therefore, predicts that interstitial hydrogen binding in boron should be insignificant, at least via interaction of  $H_2$  with boron surfaces.

**IR and XPS Spectroscopy.** Infrared spectroscopy provides a probe of B–H bonding in the milled samples, and an example spectrum is shown in Figure 3. Unfortunately, the FTIR

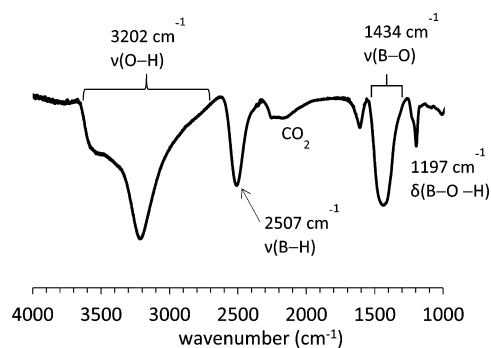


**Figure 3.** FTIR spectrum of hydrogenated boron nanoparticles produced after milling.

instrument was not equipped for inert sample introduction, and therefore this sample was exposed to air prior to analysis. The boron oxidation state in air-exposed samples was probed by X-ray photoelectron spectroscopy (XPS), as shown in Figure 4. Most of the B 1s XPS signal comes from the top ~6 nm of the boron surface (see Supporting Information), thus the appearance of a substantial peak for  $B^{3+}$  at 193 eV is consistent with the sample having a thin oxidized surface layer passivating the unoxidized core of the particles, which gives rise to the large peak for  $B^0$  at 188 eV. The B 1s binding energy for  $B^{3+}$  in materials such as  $B_2O_3$ ,  $H_3BO_3$  and various borates is quite similar,<sup>34</sup> thus XPS provides no information on the hydration state of the oxidized layer.

Consistent with the XPS result showing surface oxidation, the infrared spectrum (Figure 3) of the  $H_2$ -loaded boron is dominated by strong bands assigned to B–O stretching (1434  $cm^{-1}$ ) and O–H stretching (3202  $cm^{-1}$ ) vibrations.<sup>35</sup> The

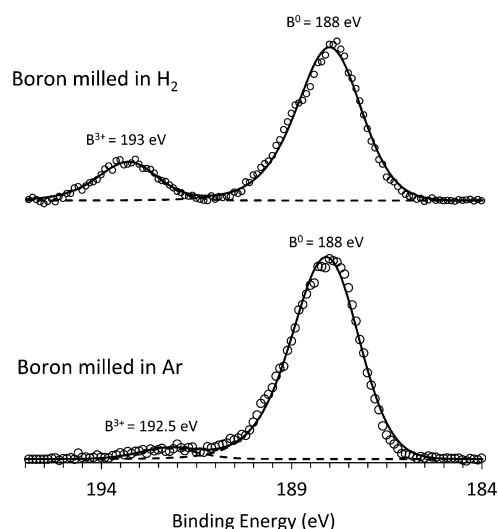


**Figure 4.** B 1s Region XPS of  $H_2$ -milled (top) and Ar-milled (bottom) boron nanoparticles exposed to air prior to analysis.

strength of the O–H stretch band suggests a significant degree of hydroxylation, i.e., the surface oxide layer appears to be partially hydrated. The IR spectrum also shows a strong peak at 2507  $cm^{-1}$  which is in the range typically seen for B–H stretching vibrations in neutral boranes<sup>36–38</sup> and other borane compounds<sup>39–42</sup> (between 2300–2700  $cm^{-1}$ ), confirming that at least some of the hydrogen is in the form of H atoms covalently bound to boron. Further confirmation that hydrogen is covalently bound to boron comes from IR spectra for samples produced by milling in  $D_2$  (Supporting Information Figure S16). There is a prominent peak at 1895  $cm^{-1}$ , which is in the range of vibrational frequencies expected for B–D bonds in deuterium substituted boranes (1850–2100  $cm^{-1}$ ).<sup>36,43</sup> The B–H stretch frequency for H atoms bound to B atoms on the surface of solid boron is not known, but might be expected to be similar to B–H stretches in boranes. The IR spectrum, therefore, does not rule out formation of boranes as the mechanism for hydrogen uptake under milling conditions, however, mass spectral evidence discussed below rules out significant production of any low molecular weight boranes which would have significant vapor pressure below 350 °C.<sup>44</sup> We cannot rule out the presence of nonvolatile boranes, although it would be surprising that these would form significantly without also forming detectable amounts of the volatile boranes. Of course, in a sense, small boron particles covered with covalently bonded H atoms are quite borane-like.

The DFT theory provides additional information for interpretation of the IR spectra. Example results are shown in Supporting Information Figures S17–S19, which show the calculated IR spectra for several  $B_{80}$  clusters with both external and interstitial H atoms. Supporting Information Figure S17 shows the spectrum of  $H@HB_{80}$ , i.e., a cluster with one interstitial and one external H atom. There is a dense band of weak transitions between ~200 and ~1300  $cm^{-1}$  corresponding to modes of the  $B_{80}$  cage, and this band is similar in all the calculated structures. There are two bands at 1416 and 2045  $cm^{-1}$  corresponding to asymmetric and symmetric stretching modes of the bridge-bonded interstitial H, and a prominent peak at ~2627  $cm^{-1}$  which is the stretch of the external B–H bond. The experimental materials have much higher hydrogen content, thus the spectra for  $H@H_{59}B_{80}$  (Supporting

Information Figure S18) and  $\text{H}@_{\text{H}_{57}}\text{B}_{80}$  (Supporting Information Figure S19) are more relevant. Both show the dense band between  $\sim 200$  and  $\sim 1300\text{ cm}^{-1}$  corresponding mostly to modes of the  $\text{B}_{80}$  cage. The boron skeletal modes are shifted to lower frequency compared to those for  $\text{H}@_{\text{HB}_{80}}$ , showing the overall weakening of the B–B skeletal bonds in the hydrogen-saturated cluster. Modes associated with terminal B–H stretching from a band between  $\sim 2550$  and  $2700\text{ cm}^{-1}$ , and modes associated with stretches of H atoms in bridging sites lie in the  $2000\text{--}2300\text{ cm}^{-1}$  range. In addition, there are peaks between  $\sim 1400$  and  $2200\text{ cm}^{-1}$  corresponding to various mixed bending+stretching motions of the hydrogen atoms, and between  $1000$  and  $1200\text{ cm}^{-1}$  there are modes which combine hydrogen bending with boron skeletal distortions. For both clusters, the modes associated with the interstitial H atoms are indicated, and found to have frequencies in the same general range as those for the external H atoms.

The experimental spectrum shows a band for B–H stretching peaking at  $2507\text{ cm}^{-1}$ , which is narrower than might be expected from the theoretical spectrum, however, this probably reflects the fact that there is considerable site-to-site variation in the stability of hydrogen chemisorption on the  $\text{B}_{80}$  cluster (Supporting Information Figure S10), which presumably is reflected in the broad range of B–H stretching frequencies. Apparently the small boron nanoparticles produced experimentally, are more homogeneous from the perspective of B–H binding. The hydrogen “bending” band calculated to lie between  $\sim 1400$  and  $2200\text{ cm}^{-1}$  presumably would also be narrower in the experimental spectrum, and may give rise to the unassigned peak near  $1600\text{ cm}^{-1}$ , but could also be obscured by the BO stretch band of the oxidized surface. The boron cage modes are calculated to give rise to a weak band between  $\sim 200$  and  $\sim 1300\text{ cm}^{-1}$ , which is not obvious in the experimental spectrum, possibly because it is simply too weak. It is also likely that in nanoparticles, this band may shift to lower frequencies, and in that case it would be out of the experimental range.

**Comparison with Boron Milled under Other Conditions.** As shown in Figure 4, the relative intensity of the  $\text{B}^{3+}$  peak in the B 1s XPS of boron that was dry-milled in  $\text{H}_2$  and subsequently exposed to air, is  $\sim 5$  times greater than that observed for boron dry-milled in argon (or  $\text{N}_2$  atmosphere) prior to air exposure. This observation indicates that the concentration of oxidized boron in the surface region of the air-exposed samples is significantly higher for the  $\text{H}_2$ -milled sample. For bulk boron, air exposure results in formation of a self-limiting oxide layer  $\sim 0.4\text{ nm}$  thick,<sup>6</sup> while XPS samples the top  $\sim 6\text{ nm}$  of the sample (see Supporting Information). The greater extent of boron oxidation for the  $\text{H}_2$ -milled sample could indicate that hydrogen loading increases thickness of the self-limiting oxide layer, perhaps by increasing the permeability of the initial oxide layer to  $\text{O}_2$ . Greater oxidation would also be explained, however, if  $\text{H}_2$ -milling changed the morphology or size distribution of the resulting particles. If, for example, the  $\text{H}_2$ -milled boron contained a larger fraction of particles in the few nanometer diameter range, the ratio of oxide layer to unoxidized core would be large, and XPS would “see through” the particles and detect a large oxide concentration. Similarly, if the  $\text{H}_2$ -milled particles were rougher, with nanometer scale asperities, then a larger fraction of the XPS-detectable surface region would oxidize on air exposure. Either scenario would also help account for the very high surface area/gram required to account for the high hydrogen uptake observed in  $\text{H}_2$ -milled boron.

The size distribution obtained in milling is determined by the balance between size reduction by crushing of particles, and particle growth by cold welding, which can occur when particles are forced together by impacts. Generally, size reduction is more efficient when wetting agents are used to help keep particles well dispersed, and to reduce cold welding.<sup>6</sup> In fact, similarly high signal for  $\text{B}^{3+}$  is also seen in XPS of boron milled under Ar or  $\text{N}_2$ , but with hexane added as a nonreactive wetting agent.<sup>6</sup> The interesting question, therefore, is whether gaseous  $\text{H}_2$  is also somehow acting as a milling agent, improving the size reduction process either by increasing the tendency for particles to fracture on impact, or by reducing cold welding via formation of a B–H surface layer.

Figure 5 compares SEM images of boron nanoparticles obtained by dry milling in  $\text{H}_2$  and Ar atmospheres. The Ar-milled nanoparticles actually appear smaller than the  $\text{H}_2$ -milled particles, however, they also have noticeably more compact,

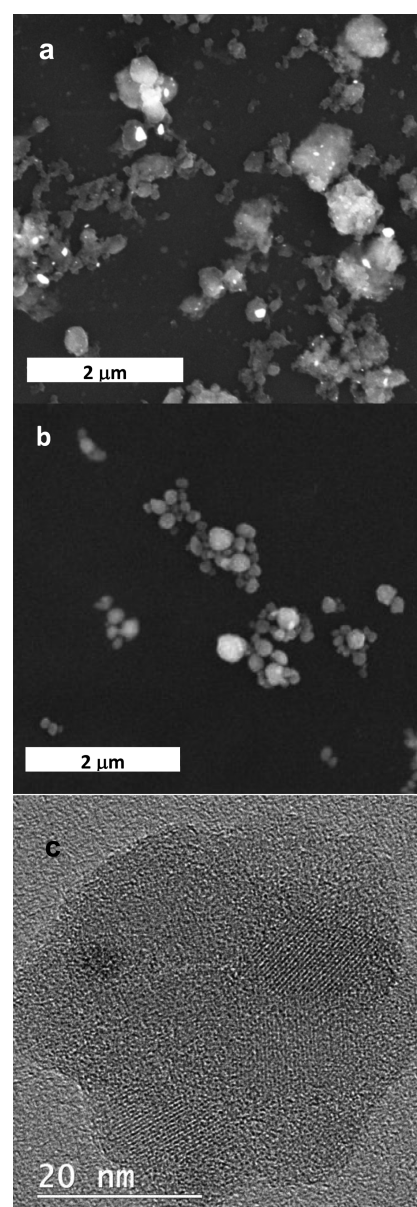


**Figure 5.** SEM images of boron nanoparticles produced from dry milling in (a)  $\text{H}_2$  atmosphere and (b) Ar atmosphere. (c) TEM image of boron nanoparticle milled in  $\text{H}_2$ .

almost spherical structures, whereas the H<sub>2</sub>-milled particles are highly irregular, with a broader size distribution, including a larger population of the smallest size particles. The highly irregular structure of the larger particles is likely a sign that these are actually aggregates of smaller, primary particles, and if the internal surfaces of these aggregates are accessible to H<sub>2</sub> and O<sub>2</sub>, this would account both for the high hydrogen uptake, and the observation of a greater extent of oxidation upon air exposure.

Boron, because it is a low *Z* element, is difficult to study in TEM, but Figure 5 also shows a TEM image of one of the small particles generated by H<sub>2</sub>-milling. Electron energy loss spectroscopy was used to verify that the particle was boron. The fact that the contrast is relatively constant across most of this particle, suggests that it has a flat, plate-like structure. More spherical particles would be thinner, with lower contrast near the edges than in the middle. The areas of higher contrast to the upper left and upper right of the particle indicate thicker regions, which are tentatively ascribed to smaller particles binding to the main particle, such that the aggregate thickness is higher. Plate-like primary particles would tend to have high surface area/volume ratio, again consistent with high hydrogen uptake, and oxidation upon air exposure.

**Mass Spectrometry of Headspace and Desorbing Gases.** As noted, both the hydrogen uptake and the appearance of B–H bonds in the IR spectrum could result either from H atoms chemisorbed on the boron particle surface, or from formation of boranes that are simply mixed with boron particles in the sample. Mass spectrometry was, therefore, used to look for the signature of boranes in the milling jar headspace gas, and also in gases evolved from the boron samples during heating. To avoid loss or destruction of low molecular weight boranes, which are volatile and reactive, the mass spectrometry experiments summarized in Figures 6 and 7 were done carefully

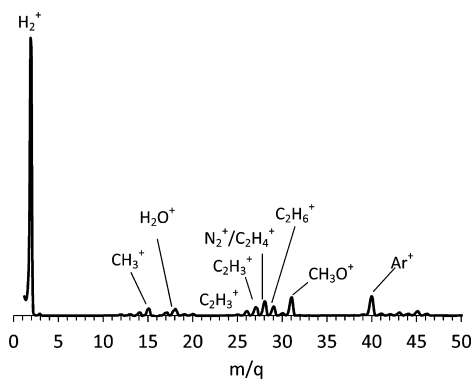


**Figure 6.** Mass spectrum of headspace gas collected from the jar after milling for 16 h.

avoiding air exposure. Figure 6 shows a typical mass spectrum of the headspace gas collected from the jar after milling in H<sub>2</sub>. For this experiment, argon was added to the initial gas mixture at a 12:1 H<sub>2</sub>:Ar ratio to have a known concentration of Ar in the headspace as an intensity standard. As expected, the headspace spectrum included prominent peaks from H<sub>2</sub> ( $m/q = 2, 1$ ) and Ar ( $m/q = 40$ ), as well as numerous small peaks attributed to organic ions, resulting from organic contaminants in the boron feedstock (see below).

There are two interesting features of the spectrum. There is a set of small peaks ( $m/q = 18, 17, 16$ ) indicating the presence of water. Some water is expected because the 95% pure boron

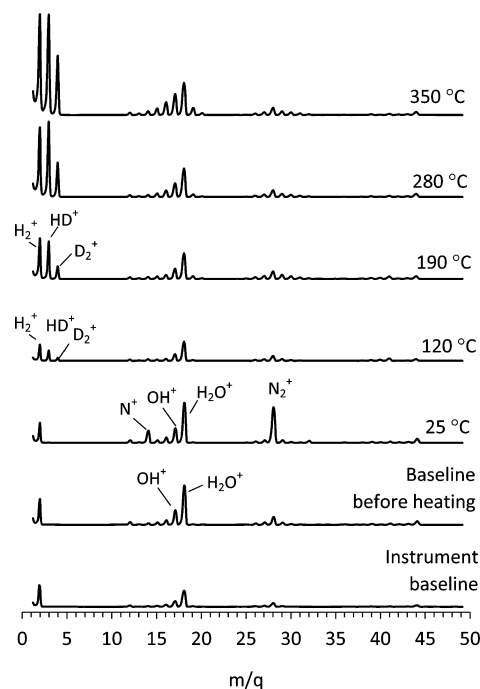


**Figure 7.** Mass spectra of gases evolved from deuterated boron nanoparticles heated to 350 °C.

feedstock is known to contain water, and there is also oxygen present on the feedstock particle surfaces that might react with H<sub>2</sub> to form water under milling conditions. Evolution of water and isotope labeling experiments are discussed below.

More importantly, the mass spectrum provides no evidence for the presence of volatile boranes. Such boranes all have characteristic patterns of peaks corresponding to stable B<sub>*x*</sub>H<sub>*y*</sub><sup>+</sup> stoichiometries, and reflecting the 5:1 <sup>11</sup>B/<sup>10</sup>B natural abundance.<sup>37</sup> For example, under electron impact conditions similar to ours, standard mass spectra of stable B<sub>*n*</sub>H<sub>*m*</sub><sup>+</sup> ( $n \leq 6$ ) compounds all show substantial peaks at  $m/q = 11$ , which is absent in our spectrum. Furthermore, the borane spectra include families of B<sub>*x*</sub>H<sub>*y*</sub><sup>+</sup> peaks that lie in  $m/q$  ranges (23–27, 33–38, 44–50) where there is essentially no signal in our spectra. We conclude, therefore, that the B–H covalent bonds observed in the IR spectrum, and the high hydrogen uptake, do not result from formation of low molecular weight boranes. This conclusion is consistent with the TC/EA and IR experiments, where volatiles would have been lost during sample transfer, which showed substantial retention of hydrogen content, and the presence of B–H bonds in the samples.

Mass spectrometry was also used to monitor gases evolved from the particles as they were heated to 350 °C, to see if any higher molecular weight borane species might be present. To help distinguish between hydrogen introduced by milling and hydrogen present as feedstock contaminants such as water and hydrocarbons, the gas evolution experiments were performed using boron milled in a D<sub>2</sub> atmosphere. The first point of interest is that uptake of D<sub>2</sub> by boron appears to be essentially identical to that of H<sub>2</sub>, as determined from pressure decreases during milling. The similarity indicates that there are no significant deuterium isotope effects on the uptake process. After preparation of the deuterium-loaded sample, the jar was opened in the glovebox, and a sample of the boron powder was placed into a glass tube, thus allowing volatiles such as D<sub>2</sub> to

escape. Volatile boranes would also have been lost, however, the results in Figure 6 show that none are produced in the hydrogen-milling process. The sample tube was valved closed in the glovebox, then connected to the mass spectrometer inlet system, which was evacuated to avoid air exposure, prior to opening the valve to allow gas sampling.

Figure 7 shows the results. At the bottom, two spectra are given showing typical instrument baseline data. The bottom spectrum, taken at the beginning of the day, shows significant signals only for hydrogen ( $m/q = 2$ ), water ( $m/q = 18, 17, 16$ ), CO/N<sub>2</sub> ( $m/q = 28$ ), and CO<sub>2</sub> ( $m/q = 44$ ). The second baseline spectrum was taken just before the start of the heating series, with elevated water signal ( $m/q = 18, 17, 16$ ) as a result of water introduction during experiments done earlier in the day. The spectrum labeled 25 °C shows the gases from the sample container before heating was started, and the only significant new signal, compared to the preheating baseline, is from glovebox nitrogen ( $m/q = 28, 14$ ) trapped in the sample container. There is no evidence of H<sub>2</sub>, HD, or D<sub>2</sub> evolving from the sample at room temperature.

The sample was then heated to 350 °C, slowly enough (5 h) to ensure that the temperature throughout the powdered sample was reasonably homogeneous. During this slow heat ramp, the gases evolved from the sample were continuously leaked into the mass spectrometer gas inlet, with mass spectra recorded at selected temperatures. Therefore, the spectra represent snapshots of the gases evolving at particular temperatures during the heat ramp. By the time the 120 °C spectrum was recorded (~30 min), the glovebox N<sub>2</sub> had largely been pumped out, as shown by negligible  $m/q = 28$  signal. In addition, the water signals also decreased by ~60% relative to the preheating baseline, reflecting a combination of loss of water from the sample, and slow recovery of the instrument baseline water signal. More importantly, the spectrum shows small signals for HD, and D<sub>2</sub> evolving from the sample. Interestingly, there is no evidence for D<sub>2</sub>O or HDO evolution at either 25 or 120 °C, where desorption of molecularly adsorbed water might be expected. This absence indicates that molecularly adsorbed water is not formed by reaction of the D<sub>2</sub> milling atmosphere with oxides or hydroxides initially present on the surface of the boron feedstock. Furthermore, we can infer that H<sub>2</sub>O, known to be present as a contaminant in the feedstock, does not undergo exchange with D bound to the boron.

As the temperature is increased, the signals for H<sub>2</sub>, HD, and D<sub>2</sub> increase significantly, dominating the mass spectra. The large H<sub>2</sub> signal is attributed to hydrogen contamination of the feedstock. HD signal indicates that isotope scrambling is reasonably efficient, which is consistent with the theoretical prediction that hydrogen is dissociatively chemisorbed to the boron surfaces, so that desorbing hydrogen is produced by recombination of H and D. At higher temperatures, small peaks at  $m/q = 19$  and 20 were observed, indicating desorption of a small amount of water produced by recombination of dissociated species such as H and OH (and isotopologs), thus allowing isotope scrambling. With increasing temperature, a number of small peaks appear in the mass ranges 12–15, 24–32, and 40–46. As shown in Supporting Information Figure S20, these clearly originate from organic contaminants in the boron feedstock, which can be removed, if necessary, by prolonged vacuum outgassing (Supporting Information Figure S21).

The results in Figure 7 show no signs of boranes evolving from the sample in the temperature range up to 350 °C. The  $m/q = 11$  signal seen for all boranes<sup>37</sup> is not observed, for example. The fragment ion patterns for deuterated boranes have not been reported to our knowledge, but would be broadened and shifted to higher mass, compared to the known spectra<sup>37</sup> for boranes. For example, the prominent B<sub>3</sub>H<sub>x</sub><sup>+</sup> ( $x = 0-5$ ) peaks seen for tetraborane and pentaborane would appear in the range  $m/q = 33$  to 43, and while there are some small peaks in this mass range, the intensity pattern is not consistent with B<sub>3</sub>D<sub>x</sub>H<sub>y</sub><sup>+</sup> ions, and suggests, instead, that the origin is fragment ions from the hydrocarbon contaminants.

**Thermogravimetric Analysis with Mass Spectrometry (TGA-MS).** To probe mass loss quantitatively and to examine gas evolution over a wider temperature range, samples prepared by milling in D<sub>2</sub> were characterized with TGA-MS, and the results are given in Figure 8. It is important to note that these

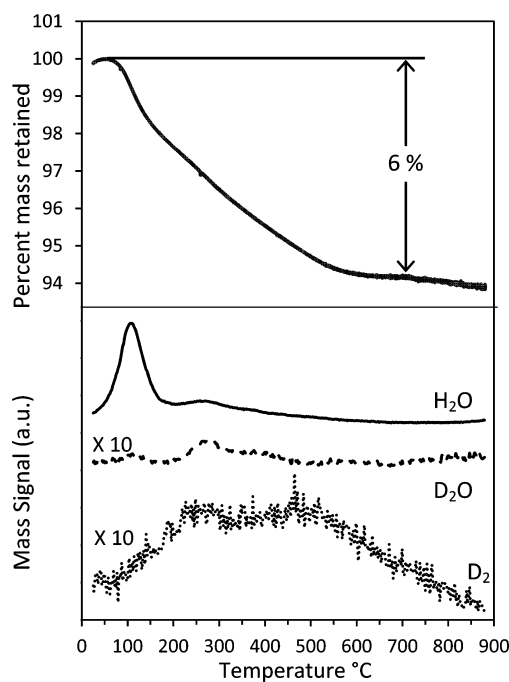


**Figure 8.** TGA profile of deuterated boron nanoparticles with corresponding desorption signal of H<sub>2</sub>O, D<sub>2</sub>O, and D<sub>2</sub> monitored through the run. TGA analysis was done inside a glovebox under inert atmosphere.

samples were never exposed to air, and TGA was done inside a nitrogen glovebox, therefore, any hydrogen- or oxygen-containing species observed in the analysis originate from the sample. The instrument has several limitations, however. It was only possible to monitor a small set of ion masses during the TGA heat ramp, which were chosen as H<sub>2</sub><sup>+</sup>, D<sub>2</sub><sup>+</sup>, H<sub>2</sub>O<sup>+</sup>, D<sub>2</sub>O<sup>+</sup>, B<sup>+</sup>, and B<sub>2</sub>D<sub>5</sub><sup>+</sup>. The latter two masses would be indicative of signal from deuterated boranes, and have little or no contribution from cracking of hydrocarbon ions. In addition, the mass spectral sensitivity of the TGA-MS instrument was found to be a strong function of mass. In particular, the sensitivity decreased rapidly at low  $m/q$ , affecting our ability to monitor H<sub>2</sub> and D<sub>2</sub> evolution. No signal was observed for H<sub>2</sub><sup>+</sup>, even though the mass spectra in Figure 7, where sensitivity was calibrated, show this to be a major product ion. The signal for D<sub>2</sub><sup>+</sup> was sufficient to allow TGA-MS measurements, but



comparison with Figure 7 indicates that the  $D_2^+$  sensitivity is at least 25 times lower than that for  $H_2O^+$ , which was the most intense mass spectral signal observed.

The top frame of Figure 8 shows the percent mass change versus temperature, and the raw ion intensities for  $D_2^+$ ,  $D_2O^+$ , and  $H_2O^+$  are shown in the bottom frame. A rapid  $\sim 1.5\%$  mass loss was observed between  $\sim 100$  and  $150$  °C, and the mass spectral results suggest that  $\sim 1\%$  corresponds to desorption of undeuterated water attributed to water in the boron feedstock. A somewhat slower mass loss continued as the sample was heated up to  $900$  °C, totaling  $\sim 6\%$ , that is,  $\sim 5\%$  mass loss if the contribution from water is subtracted. The pressure drop during production of this sample was consistent with  $\sim 6$  wt % deuterium loading, thus the mass loss, not including water, was about 1% less than expected. This may simply indicate that higher temperatures would be required to lose all the deuterium. The mass spectral results (Figure 7) indicate that the primary loss was of  $D_2$ , HD, and  $H_2$ , although only  $D_2$  could be monitored in the TGA-MS. The  $D_2$  desorption temperature dependence shows evidence of two broad features, peaking at  $\sim 270$  °C and  $\sim 480$  °C. These have previously been attributed to recombinative desorption from sites with terminal B–D and bridging B–D–B bonds, respectively,<sup>13</sup> although the FTIR results above show no evidence for bridge-bonded hydrogen, and the theory also suggests that terminal bonding is both more important and more stable. Clearly, the hydrogen loaded into boron by milling is strongly bonded, with temperatures approaching  $900$  °C required to desorb it. The high desorption temperature would clearly be problematic for hydrogen storage, however, for propellants or fuels, the strong B–H binding is advantageous, ensuring that the hydrogen is not lost during storage. Under combustion conditions, the hydrogen would be consumed as the boron burned, resulting in an increase in  $I_{sp}$  due to additional low molecular weight products. There is also the possibility that presence of hydrogen on the boron surface might significantly enhance ignition, because, by analogy with boranes, the B–H bonds are likely to be reactive with oxidizers.

The  $D_2O$  intensity trace is also interesting. During the strong initial pulse of water desorption around  $120$  °C, there is little if any  $D_2O$  desorption, however, there are also weak water desorption features between  $\sim 250$  and  $400$  °C, and both  $H_2O$  and  $D_2O$  are observed in these. These TGA-MS results are consistent with the conclusion reached above, that milling in  $D_2$  does not result in significant production of molecularly adsorbed deuterated water, thus the water signal around  $120$  °C, corresponding to desorption of this molecularly adsorbed water, shows no isotope exchange. The higher temperature desorption features correspond to recombinative desorption, where H/D scrambling is facile. This two stage water desorption behavior is somewhat reminiscent of water desorption from boric acid ( $H_3BO_3$ ).<sup>45</sup>

**Reactivity with Oxygen.** Reactivity of hydrogenated boron nanoparticles with oxygen was investigated by monitoring mass gain as samples were heated under an  $O_2$  gas flow using a TGA system. Figure 9 compares results for samples of hydrogen-milled and argon-milled boron. For Ar-milled boron, the sample mass was essentially constant up to about  $100$  °C, and then there was a slow increase totaling  $\sim 1\%$  as the temperature was ramped up to  $\sim 400$  °C. At that point, the rate of mass gain increased, reaching a maximum at  $500$  °C, before tapering off above  $\sim 550$  °C. For this sample, which was transferred to the TGA in air, the boron particles were coated and passivated by a

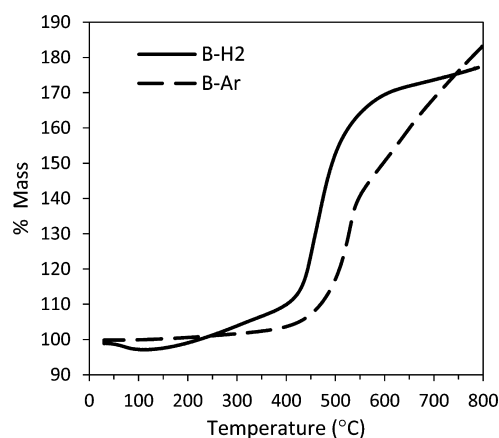


**Figure 9.** TGA analysis of boron milled in  $H_2$  and Ar run under  $O_2$  atmosphere.

thin oxide layer, as shown by the XPS results in Figure 4. For temperatures well below the  $B_2O_3$  melting temperature ( $450$  °C), slow mass gain is expected because diffusion of oxygen through the passivating oxide layer is slow. As the oxide approaches and passes its melting point, oxygen diffusion becomes fast, and the oxide layer grows at an increasing rate, with concomitant increase in mass. The temperature range probed is well below the oxide sublimation temperature ( $1500$  °C) thus the oxidation products remain on the particle surface, thickening the oxide layer, and leading to eventual slowing of the mass gain rate.

The  $H_2$ -milled sample used in this experiment had  $\sim 3.5$  wt % of hydrogen uptake. The XPS data in Figure 4 shows that when such  $H_2$ -milled samples are exposed to air during sample transfer, the fraction of oxidized boron in the surface region is substantially greater than in the Ar-milled sample. This increased oxidation could indicate that incorporated hydrogen increases reactivity toward oxygen, but also could reflect increased surface area (Figure 5). When hydrogenated boron oxidizes in air, it could form  $B_2O_3$  (as in unhydrogenated boron), but one might expect that the surface would consist of hydrated forms of the oxide, such as  $H_3BO_3$ ,  $HBO_2$ , or  $H_2B_4O_7$ , which form in oxidation of boranes.<sup>46,47</sup> The presence of some degree of hydration is confirmed by the strong OH stretching signal observed in the IR spectrum of oxidized,  $H_2$ -milled boron (Figure 3).

As such a sample is heated, the surface layer would tend to dehydrate, leading to an initial mass loss, and just such an initial mass loss of 3% is observed as the sample was heated to  $100$  °C. Note, however, that the mass loss stops well below the temperature expected for complete dehydration to  $B_2O_3$  ( $250$  °C for bulk boron oxide), and mass begins to increase again above  $100$  °C. Furthermore, the rate of mass gain in the  $100$  °C to  $\sim 420$  °C temperature range is five times faster than the rate observed for the Ar-milled sample. Faster oxidation of the  $H_2$ -milled boron is attributed to some combination of higher reactivity of the hydrogen-loaded boron, and higher surface area. For the  $H_2$ -milled sample, the transition to rapid mass gain occurs at  $\sim 420$  °C, compared to  $\sim 500$  °C for Ar-milled boron, and in addition, the transition is more abrupt and the subsequent rate of mass gain is faster than for the Ar-milled sample. All three of these factors suggest that the changes in surface properties resulting from  $H_2$  milling, should lead to more facile ignition of  $H_2$ -milled boron under combustion conditions.

**Effects of Hydrogenation on Performance as a Fuel Additive.** The specific impulse,  $I_{sp}$ , is a measure of the amount of thrust obtainable in rocket propulsion from a given mass of fuel.  $I_{sp}$  is proportional to the exhaust velocity and, therefore, depends on the distribution of molecular weights of the combustion products as well as the exhaust temperature. Hydrogen addition tends to generate lower molecular weight products, and should improve  $I_{sp}$ . To estimate the potential impact of hydrogen loading, the  $I_{sp}$  of hydrogenated boron was calculated using the U.S. Air Force  $I_{sp}$  computational model.<sup>21</sup> Specific impulse values were calculated for the system at standard conditions; that is, chamber pressure was set at 1000 psi, engine exhaust was set to sea level pressure through an optimized nozzle expansion.<sup>48</sup> The heat of formation and physical property input data for oxidizer and fuels for the calculations were from the literature.<sup>49,50</sup> The physical model of the hydrogenated boron particles assumes hydrogen is taken up through covalent bonds to boron atoms to form a borane-like shell (modeled as decaborane) over an elemental boron core. For hydrogenated boron particles with 5 wt % hydrogen content, the core/shell ratio is 56.7:43.3.

The theoretical  $I_{sp}$  was calculated to be 276 s for a bipropellant baseline system consisting of a kerosene-based fuel (RP1) and the liquid storable oxidizer, dinitrogen tetroxide (NTO). In comparison, theoretical performance of a bipropellant system incorporating 10% concentration of 5 wt % hydrogenated boron in the RP1 fuel is 280 s. An additional calculation was conducted with fully hydrogenated particles (essentially decaborane) and for the same 10% concentration, a specific impulse of 284.5 s was obtained. Thus, as the degree of hydrogenation of the particles increases, there is some increase in  $I_{sp}$ , as expected, however the effect is not dramatic. As pointed out above, however, there is also the possibility that hydrogenating the boron to create a borane-like surface, might substantially increase the reactivity toward oxidizers, and therefore improve the ignition and combustion properties of the fuel. Some suggestion of this effect is observed in Figure 9, where oxidation begins at lower temperature and is more rapid, than for Ar-milled boron.

As a first test of this possibility, we examined the effects of small loadings of hydrogenated boron on the hypergolic ignition of two ionic liquids, using methods we have previously reported.<sup>31</sup> 1-butyl-3-methyl-imidazolium dicyanamide ([BMIM][DCA]) and 1-methyl-4-amino-1,2,4-triazolium dicyanamide ([MAT][DCA]), were added under an Ar atmosphere to preweighed flasks containing both H<sub>2</sub>-milled (B-H<sub>2</sub>) and D<sub>2</sub>-milled (B-D<sub>2</sub>) boron nanoparticles. The sealed 0.3 wt % mixtures ultrasonicated until no nanoparticles were visible at the bottom of the vial. The resulting suspensions appeared slightly opaque relative to the clear, slightly yellow color of the neat ILs. The suspended B-H<sub>2</sub> and B-D<sub>2</sub> nanoparticles began settling out after ~24 h from [BMIM][DCA] and after ~36 h from [MAT][DCA] with no difference in suspension stability whether the boron particles were milled under H<sub>2</sub> or D<sub>2</sub>. Once settling was observed, samples could be redispersed through the same process. The enhanced suspension stability for [MAT][DCA] vs [BMIM][DCA] was also observed for boron nanoparticles milled in, and capped with [MAT][DCA], as previously reported.<sup>31</sup>

It is interesting to note that the boron samples milled under H<sub>2</sub> were not only less stable in these ILs than boron nanoparticles milled in the presence of [MAT][DCA] without H<sub>2</sub>,<sup>31</sup> but that resuspending the B-H<sub>2</sub> nanoparticles required

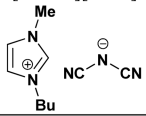
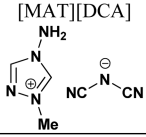
ultrasonication, while boron nanoparticles milled in [MAT][DCA] stayed suspended longer and required only simple vortex mixing after settling. The difference is attributed to differences in the surface chemistry of the particles. Particles milled in [MAT][DCA] (or [BMIM][DCA]) are capped with a layer of the IL that is bound strongly enough to resist vigorous solvent washing, and to protect the particle surface from air oxidation. Zeta potential measurements show that the particles are charged by binding of MAT<sup>+</sup> in the case of [MAT][DCA], and of DCA<sup>-</sup> in the case of [BMIM][DCA].<sup>8</sup> As shown above, the hydrogen-milled particles are simply capped with a layer of covalently bound H atoms, and the H-capped particles are obviously less IL-compatible than the charged, IL-capped boron.

While suspended, the B-H<sub>2</sub> nanoparticle-loaded ILs were tested for hypergolic ignition. A 10  $\mu$ L aliquot of the IL fuel was dropped into a vial containing 500  $\mu$ L of white fuming nitric acid (WFNA)<sup>30,31</sup> and the resulting ignition was monitored with a high speed camera (Supporting Information Figures S22–S25). Upon contact with the WFNA, the neat samples of [BMIM][DCA] and [MAT][DCA] resulted in a single ignition with an ignition delay of 41 and 34 ms, respectively (Table 1). Samples tested with 0.3 wt % B-H<sub>2</sub> loading had ignition delays that were identical to those for the neat ILs, within the measurement uncertainties, however, there were changes in the ignition and combustion characteristics, as discussed below.

B-H<sub>2</sub> in [BMIM][DCA] led to more vigorous combustion, as shown by an improved flame height (from 4 to 5 cm), a much longer overall flame duration, and the observation of multiple flames. Both the insensitivity of ignition delay to the presence of a small particle loading, and the observations of altered flame characteristics, closely match our previous reports of this IL loaded with boron nanoparticles milled in [MAT][DCA] (Table 1).<sup>31</sup> After essentially the same ignition delay as the neat IL, the resulting ignition was more powerful with a higher flame (>10 cm) and a single combustion process (Table 1).

Taken together with our previous studies,<sup>31</sup> these results suggest that the surface functionalization of the boron nanoparticles is important in providing additional stability of the suspensions. The lower suspension stability of the H<sub>2</sub>-milled vs [MAT][DCA]-milled boron nanoparticles, must be balanced with the ease and lower cost of milling under H<sub>2</sub> vs milling in ILs. The other conclusion is that the reactivity of the ILs with H<sub>2</sub>-milled nanoparticles is not very different from ILs containing nanoparticles milled in the IL. It is not surprising that the ignition delays of these 0.3 wt % samples are not significantly different from those of the neat ILs, because the initial contact with the oxidizer is by the IL, rather than the suspended particles, and the boron presumably does not begin to oxidize until ignition of the IL exposes the particles. The fact that there are effects on flame height and duration suggest that the boron does enhance combustion, and this enhancement may involve both combustion of the boron, but also possible effects such as combustion catalysis on the particle surfaces and improvements in heating rates due to radiative heating of the particles (which appear black in higher concentration suspensions). To test the inherent combustibility of the boron particles, experiments at much higher particle loadings are needed.

**Table 1. Summary of Ignition and Combustion Properties of Neat [BMIM][DCA] and [MAT][DCA] ILs and the Same ILs with Several Types of Boron Nanoparticles Added at 0.3% Loading<sup>c</sup>**

Compound	Colloidal Stability (h)	Ignition Delay <sup>a</sup> (ms)	Ignition Duration (ms)	Notes
[BMIM][DCA] 	N/A	41(1) <sup>b</sup>	110(40)	One Flame – Medium
0.3% B-H <sub>2</sub>	24	42(2)	159(56)	Two Flames – Medium and Medium
Neat [BMIM][DCA] <sup>a</sup>	N/A	44(2)	106(6)	One Flame – Medium
0.33% B no ligand <sup>d</sup>	<24	44(3)	108(41)	One Flame – Very weak
0.33% B surfactant <sup>d</sup>	24	43(3)	110(50)	Two Flames – Medium
0.33% B [MAT][DCA] <sup>a</sup>	48	44(3)	130(31)	Three Flames – Medium and High
[MAT][DCA] 	N/A	34(10)	59(10)	One Flame – Medium
0.3% B-H <sub>2</sub>	36	34(2)	87(10)	One Flame – Very Strong
Neat [MAT][DCA] <sup>a</sup>	N/A	37(6)	77(18)	One Flame – Medium
0.33% B no ligand <sup>d</sup>	<24	43(9)	52(12)	One/Two Flames – Very weak
0.33% B surfactant <sup>d</sup>	24	45(11)	56(7)	One Flame – Medium
0.33% B [MAT][DCA] <sup>a</sup>	48	45(14)	43(4)	One Flame – Very Strong

<sup>a</sup>Data taken from ref 32. <sup>b</sup>Numbers in parenthesis denote calculated standard deviations. <sup>c</sup>The numbers in parentheses following the ignition delay and duration values are the standard deviations of multiple runs. The results for H<sub>2</sub>-loaded boron particles are compared to previous work for the same ILs loaded with non-hydrogenated boron nanoparticles, with and without capping by either a hydrocarbon ligand or by [MAT][DCA].<sup>32</sup>

## CONCLUSION

Boron nanoparticles were prepared and loaded with hydrogen using ball milling, with the result that as much as 5 wt % (36 mol %) of hydrogen can be loaded into boron nanoparticles. Mass spectrometry and TGA experiments show that the incorporated hydrogen is stable up to ~100 °C. DFT calculations predict that hydrogen dissociatively adsorbs on the particle surfaces, mostly via terminal B–H bonds, and that interstitial binding is significantly higher in energy and therefore not likely to be important. FTIR experiments are consistent with this prediction, showing evidence only of terminal B–H covalent bonding, similar to that observed in boranes. Mass spectroscopy and TGA-MS analyses show no evidence for formation of molecular boranes that are volatile in the temperature range probed.

Given that the boron–hydrogen binding appears to involve only B–H bonds to the surface, very high surface areas are required to account for the high hydrogen loadings observed. SEM and TEM suggest that the boron primary particles are

small, with plate-like geometries that would, indeed, result in high surface areas. It appears that in H<sub>2</sub>-milling the formation of a B–H layer on the boron surfaces acts to improve size reduction, by some combination of enhanced fracturing and reduced cold-welding probabilities.

Thermal desorption experiments showed that hydrogen desorbs mostly by recombination to produce H<sub>2</sub>, with a smaller amount desorbing from oxidized samples as H<sub>2</sub>O formed by recombination and desorption from hydrated oxides. Under inert atmosphere, most of the hydrogen desorbs from the boron below ~550 °C, although some desorption continues to 900 °C. Together with the observation that H<sub>2</sub>-milled boron also oxidizes more readily than boron without hydrogen loading, this result suggests that hydrogen-loaded boron might significantly improve ignition, and combustion, as well as providing a small increase in *I*<sub>sp</sub>. Enhancements in flame height and duration suggest that the particles do burn during the hypergolic ignition of boron–IL suspensions.

## ASSOCIATED CONTENT

### Supporting Information

Additional XPS, MS, FTIR, combustion data, and DFT calculations. This material is available free of charge via the Internet at <http://pubs.acs.org/>.

## AUTHOR INFORMATION

### Corresponding Author

\*E-mail: anderson@chem.utah.edu.

### Author Contributions

S.S., J.A.B., T.W.H., R.D.R., and S.L.A. are senior authors.

### Notes

The authors declare no competing financial interest.

## ACKNOWLEDGMENTS

The authors acknowledge support from the Air Force Office of Scientific Research under AFOSR MURI Grant FA9550-08-1-0400 and BRI Grant FA9550-12-1-0481, and from the University of Utah Research Foundation (grant 51003387). This work made use of University of Utah shared facilities of the Micron Microscopy Suite sponsored by the College of Engineering, Health Sciences Center, Office of the Vice President for Research, and the Utah Science Technology and Research (USTAR) initiative of the State of Utah. The AFRL group would like to acknowledge the Department of Defense High Performance Computing Modernization Program at the Air Force Research Laboratory, Engineering Research and Development Center, and Navy DoD Supercomputing Resource Centers for the computer time granted for the theoretical work. The University of Alabama group would like to thank the Air Force Office of Scientific Research (AFOSR Grant FA9550-10-1-0521), and P.D.M. thanks the United States Department of Defense (DoD) through the National Defense, Science & Engineering Graduate Fellowship (NDSEG) Program.

## REFERENCES

- (1) Cox, J. D.; Wagman, D. D.; Medvedev, V. A. *Codata Key Values for Thermodynamics*; Hemisphere Publishing Corp.: New York, 1984.
- (2) Plantier, K. B.; Pantoya, M. L.; Gash, A. E. Combustion Wave Speeds of Nanocomposite Al/Fe<sub>2</sub>O<sub>3</sub>: The Effects of Fe<sub>2</sub>O<sub>3</sub> Particle Synthesis Technique. *Combust. Flame* **2005**, *140*, 299–309.

- (3) Armstrong, R. W.; Baschung, B.; Booth, D. W.; Samirant, M. Enhanced Propellant Combustion with Nanoparticles. *Nano Lett.* **2003**, *3*, 253–255.
- (4) Wang, L. L.; Munir, Z. A.; Maximov, Y. M. Review Thermite Reactions: Their Utilization in the Synthesis and Processing of Materials. *J. Mater. Sci.* **1993**, *28*, 3693–3708.
- (5) Van Devener, B.; Perez, J. P. L.; Anderson, S. L. Air-Stable, Unoxidized, Hydrocarbon-Dispersible Boron Nanoparticles. *J. Mater. Res.* **2009**, *24*, 3462–3464.
- (6) Van Devener, B.; Perez, J. P. L.; Jankovich, J.; Anderson, S. L. Oxide-Free, Catalyst-Coated, Fuel-Soluble, Air-Stable Boron Nanopowder as Combined Combustion Catalyst and High Energy Density Fuel. *Energy Fuels* **2009**, *23*, 6111–6120.
- (7) Perez, J. P. L.; McMahan, B. W.; Anderson, S. L. Functionalization and Passivation of Boron Nanoparticles with a Hypergolic Ionic Liquid. *J. Propul. Power* **2013**, *29*, 489–495.
- (8) Perez, J. P. L.; McMahan, B. W.; Schneider, S.; Boatz, J. A.; Hawkins, T. W.; McCrary, P. D.; Beasley, P. A.; Kelley, S. P.; Rogers, R. D.; Anderson, S. L. Exploring the Structure of Nitrogen-Rich Ionic Liquids and Their Binding to the Surface of Oxide-Free Boron Nanoparticles. *J. Phys. Chem. C* **2013**, *117*, 5693–5707.
- (9) Dequasia, A. T. *The Green Flame: Surviving Government Secrecy*; American Chemical Society: Washington, DC, 1991.
- (10) Eberle, U.; Felderhoff, M.; Schueth, F. Chemical and Physical Solutions for Hydrogen Storage. *Angew. Chem., Int. Ed.* **2009**, *48*, 6608–6630.
- (11) Khalil, A. E. E.; Gupta, A. K. Hydrogen Addition Effects on High Intensity Distributed Combustion. *Appl. Energy* **2013**, *104*, 71–78.
- (12) Weng, Q.; Wang, X.; Zhi, C.; Bando, Y.; Golberg, D. Boron Nitride Porous Microbelts for Hydrogen Storage. *ACS Nano* **2013**, *7*, 1558–1565.
- (13) Wang, P.; Orimo, S.; Tanabe, K.; Fujii, H. Hydrogen in Mechanically Milled Amorphous Boron. *J. Alloys Compd.* **2003**, *350*, 218–221.
- (14) Tilton, J. A.; Smith, W. M.; Hockerberger, W. G. Production of High Cetane Number Diesel Fuels by Hydrogenation. *Ind. Eng. Chem. Res.* **1948**, *40*, 1269–1273.
- (15) Ji, C.; Wang, S.; Zhang, B. Performance of a Hybrid Hydrogen–Gasoline Engine under Various Operating Conditions. *Appl. Energy* **2012**, *97*, 584–589.
- (16) Clayton, R. M. Hydrogen Enrichment for Low-Emission Jet Combustion. *Adv. Chem. Ser.* **1978**, *166*, 267–286.
- (17) Ghenai, C.; Zbeeb, K.; Janajreh, I. Combustion of Alternative Fuels in Vortex Trapped Combustor. *Energy Convers. Manage.* **2013**, *65*, 819–828.
- (18) Ma, F.; Wang, Y.; Liu, H.; Li, Y.; Wang, J.; Zhao, S. Experimental Study on Thermal Efficiency and Emission Characteristics of a Lean Burn Hydrogen Enriched Natural Gas Engine. *Int. J. Hydrogen Energy* **2007**, *32*, S067–S075.
- (19) Guo, H.; Hosseini, V.; Neill, W. S.; Chippior, W. L.; Dumitrescu, C. E. An Experimental Study on the Effect of Hydrogen Enrichment on Diesel Fueled Hcci Combustion. *Int. J. Hydrogen Energy* **2011**, *36*, 13820–13830.
- (20) Department of Energy Hydrogen and Fuel Cells Program Plan; U.S. Department of Energy: Washington, DC, 2011.
- (21) Beckman, C.; Acree, R.; Magee, T. *USAF Theoretical ISP Program*; U.S. Air Force Research Laboratory: Edwards AFB, CA, 1990.
- (22) Zhao, J.; Wang, L.; Li, F.; Chen, Z. B80 and Other Medium-Sized Boron Clusters: Core–Shell Structures, Not Hollow Cages. *J. Phys. Chem. A* **2010**, *114*, 9969–9972.
- (23) Li, F.; Jin, P.; Jiang, D.; Wang, L.; Zhang, S. B.; Zhao, J.; Chen, Z. B80 and B101–103 Clusters: Remarkable Stability of the Core–Shell Structures Established by Validated Density Functionals. *J. Chem. Phys.* **2012**, *136*, 074302–074311.
- (24) Zhao, Y.; Truhlar, D. G. The M06 Suite of Density Functionals for Main Group Thermochemistry, Thermochemical Kinetics, Non-covalent Interactions, Excited States, and Transition Elements: Two New Functionals and Systematic Testing of Four M06-Class Functionals and 12 Other Functionals. *Theor. Chem. Acc.* **2008**, *120*, 215–241.
- (25) Krishnan, R.; Binkley, J. S.; Seeger, R.; Pople, J. A. Self-Consistent Molecular Orbital Methods. XX. A Basis Set for Correlated Wave Functions. *J. Chem. Phys.* **1980**, *72*, 650–654.
- (26) Clark, T.; Chandrasekhar, J.; Spitznagel, G. W.; Schleyer, P. v. R. Efficient Diffuse Function-Augmented Basis Sets for Anion Calculations. III. The 3-21+G Basis Set for First-Row Elements, Li–F. *J. Comput. Chem.* **1983**, *4*, 294–301.
- (27) Schmidt, M. W.; Baldridge, K. K.; Boatz, J. A.; Elbert, S. T.; Gordon, M. S.; Jensen, J. H.; Koseki, S.; Matsunaga, N.; Nguyen, K. A.; Su, S.; Windus, T. L.; Dupuis, M.; Montgomery, J. A. General Atomic and Molecular Electronic Structure System. *J. Comput. Chem.* **1993**, *14*, 1347–1363.
- (28) Gordon, M. S.; Schmidt, M. W. In *Theory and Applications of Computational Chemistry: The First Forty Years*; Dykstra, C. E., Frenking, G., Kim, K. S., Scuseria, G. E., Eds.; Elsevier: Amsterdam, 2005; pp 1167–1189.
- (29) Valiev, M.; Bylaska, E. J.; Govind, N.; Kowalski, K.; Straatsma, T. P.; van Dam, H. J. J.; Wang, D.; Nieplocha, J.; Apra, E.; Windus, T. L.; de Jong, W. A. NWChem: A Comprehensive and Scalable Open-Source Solution for Large Scale Molecular Simulations. *Comput. Phys. Commun.* **2010**, *181*, 1477–1489.
- (30) Schneider, S.; Hawkins, T.; Rosander, M.; Vaghjiani, G.; Chambreau, S.; Drake, G. Ionic Liquids as Hypergolic Fuels. *Energy Fuels* **2008**, *22*, 2871–2872.
- (31) McCrary, P. D.; Beasley, P. A.; Cojocar, O. A.; Schneider, S.; Hawkins, T. W.; Perez, J. P. L.; McMahan, B. W.; Pfiel, M.; Boatz, J. A.; Anderson, S. L.; Son, S. F.; Rogers, R. D. Hypergolic Ionic Liquids to Mill, Suspend, and Ignite Boron Nanoparticles. *Chem. Commun.* **2012**, *48*, 4311–4313.
- (32) Huang, Z.; Calka, A.; Liu, H. DSC Study of the Effect of Milling Conditions on the Hydrogen Storage Properties of Boron. *J. Mater. Sci.* **2007**, *42*, 3985–3989.
- (33) Kobayashi, M.; Higashi, I.; Takami, M. Fundamental Structure of Amorphous Boron. *J. Solid State Chem.* **1997**, *133*, 211–214.
- (34) Moulder, J. F.; Stickle, W. F.; Sobol, P. E.; Bomben, K. D. *Handbook of X-Ray Photoelectron Spectroscopy*; Chastain, J., King, R. C., Jr., Eds.; Physical Electronics: Eden Prairie, MN, 1995.
- (35) Peak, D.; Luther, G. W. I.; Sparks, D. L. ATR-FTIR Spectroscopic Studies of Boric Acid Adsorption on Hydrous Ferric Oxide. *Geochim. Cosmochim. Acta* **2003**, *67*, 2551–2560.
- (36) Lord, R. C.; Nielsen, E. The Vibrational Spectra of Diborane and Some of Its Isotopic Derivatives. *J. Chem. Phys.* **1951**, *19*, 1–10.
- (37) Linstrom, P. J.; Mallard, W. G. *NIST Chemistry Webbook, NIST Standard Reference Database Number 69*; National Institute of Standards and Technology: Gaithersburg, MD, 2011.
- (38) Kawaguchi, K. Fourier Transform Infrared Spectroscopy of the B<sub>h</sub> 3 Band. *J. Chem. Phys.* **1992**, *96*, 3411–3415.
- (39) Concha, B. M.; Chatenet, M.; Maillard, F.; Ticianelli, E. A.; Lima, F. H. B.; de Lima, R. B. In Situ Infrared (FTIR) Study of the Mechanism of Borohydride Oxidation Reaction. *Phys. Chem. Chem. Phys.* **2010**, *12*, 11507–11516.
- (40) Lehmann, W. J.; Wilson, C. O.; Shapiro, I. Infrared Spectra of Alkyldiboranes. I. Monomethyldiborane. *J. Chem. Phys.* **1960**, *32*, 1088–1093.
- (41) Li, L.; Gu, Q.; Tang, Z.; Chen, X.; Tan, Y.; Li, X. Two Novel Derivatives of Ammonia Borane for Hydrogen Storage: Synthesis, Structure, and Hydrogen Desorption Investigation. *J. Mater. Chem. A* **2013**, *1*, 12263–12269.
- (42) Leites, L. A. Vibrational Spectroscopy of Carboranes and Parent Boranes and Its Capabilities in Carborane Chemistry. *Chem. Rev.* **1992**, *92*, 279–323.
- (43) Gennari, F. C.; L, A. F.; Rios, I. J. Synthesis and Thermal Stability of Zr(Bh<sub>4</sub>)<sub>4</sub> and Zr(Bd<sub>4</sub>)<sub>4</sub> Produced by Mechanochemical Processing. *Inorg. Chim. Acta* **2009**, *362*, 3731–3737.
- (44) Yaws, C. L. *Handbook of Vapor Pressure*; Gulf Publishing Co.: Houston, TX, 1995; p 4.

- (45) Balci, S.; Sezgi, N. A.; Eren, E. Boron Oxide Production Kinetics Using Boric Acid as Raw Material. *Ind. Eng. Chem. Res.* **2012**, *51*, 11091–11096.
- (46) Roth, W.; Bauer, W. H. The Explosive Oxidation of Diborane. *J. Phys. Chem.* **1956**, *60*, 639–641.
- (47) Ludlum, K. H.; Wiberley, S. E.; Bauer, W. H. The Oxidation of Tetraborane. Ph.D. Dissertation, Rensselaer Polytechnic Institute, Troy, NY, 1961.
- (48) Sutton, G. P. *Rocket Propulsion Elements*, 6th ed.; Wiley: New York, 1992.
- (49) Johnson, W. H.; Kilday, M. V.; Prosen, E. J. Heat of Formation of Decaborane. *J. Res. Natl. Bur. Stand., Sect. A* **1960**, *64A*, 521–525.
- (50) Edwards, T. Liquid Fuels and Propellants for Aerospace Propulsion: 1903–2003. *J. Propul. Power* **2003**, *19*, 1089–1107.